New constraints on sterile neutrino dark matter from NuSTAR M31 observations

Kenny C. Y. Ng,[1,*] Brandon M. Roach,[2,†] Kerstin Perez,[2,‡] John F. Beacom,[3,4,5,§] Shunsaku Horiuchi,[6,‖] Roman Krivonos,[7,¶] and Daniel R. Wik[8,**]

[1]*Department of Particle Physics and Astrophysics, Weizmann Institute of Science, Rehovot 76100, Israel*
[2]*Department of Physics, Massachusetts Institute of Technology, Cambridge, Massachusetts 02139, USA*
[3]*Center for Cosmology and AstroParticle Physics (CCAPP), The Ohio State University, Columbus, Ohio 43210, USA*
[4]*Department of Physics, The Ohio State University, Columbus, Ohio 43210, USA*
[5]*Department of Astronomy, The Ohio State University, Columbus, Ohio 43210, USA*
[6]*Center for Neutrino Physics, Department of Physics, Virginia Tech, Blacksburg, Virginia 24061, USA*
[7]*Space Research Institute of the Russian Academy of Sciences (IKI), Moscow, Russia, 117997*
[8]*Department of Physics and Astronomy, University of Utah, Salt Lake City, Utah 84112, USA*

(Received 17 January 2019; published 10 April 2019)

We use a combined 1.2 Ms of NuSTAR observations of M31 to search for x-ray lines from sterile neutrino dark matter decay. For the first time in a NuSTAR analysis, we consistently take into account the signal contribution from both the focused and unfocused fields of view. We also reduce the modeling systematic uncertainty by performing spectral fits to each observation individually and statistically combining the results, instead of stacking the spectra. We find no evidence of unknown lines, and thus derive limits on the sterile neutrino parameters. Our results place stringent constraints for dark matter masses $\gtrsim$12 keV, which reduces the available parameter space for sterile neutrino dark matter produced via neutrino mixing (e.g., in the νMSM) by approximately one-third. Additional NuSTAR observations, together with improved low-energy background modeling, could probe the remaining parameter space in the future. Lastly, we also report model-independent limits on generic dark matter decay rates and annihilation cross sections.

DOI: 10.1103/PhysRevD.99.083005

I. INTRODUCTION

Numerous lines of evidence from gravitational signatures point to the existence of beyond the Standard Model matter—dark matter (DM)—that constitutes more than 5 times the cosmic energy density of baryons [1–3]. The identification of DM is an important task in modern science and could lead to the resolution of many outstanding problems in particle physics and cosmology.

A powerful DM search strategy is to look for signatures of DM decaying or annihilating into visible products, i.e., indirect detection. In particular, channels with monoenergetic photons in the final state are powerful search modes due to the efficient separation of signal and background, as the latter is often dominated by a smooth continuum emission.

Many well-motivated DM candidates could lead to line signatures. In the x-ray band, one of the most studied candidates is sterile neutrinos [4–7], which can radiatively decay into an active neutrino and a monoenergetic photon ($\chi \to \gamma + \nu$) with energy equal to half of the DM mass [8–11]. The production of sterile neutrino DM can be naturally achieved in the early Universe via a small mixing with active neutrinos [12], which may be enhanced by the presence of primordial lepton asymmetry [13]. As the mixing angle determines both the abundance and decay rate, there is a finite window in the mass-mixing angle parameter plane in which sterile neutrinos could constitute the full DM abundance, thus allowing this scenario to be fully testable. Closing this window would imply additional physics and production mechanisms are needed to make sterile neutrinos a viable DM candidate [14–21]. The existence of sterile neutrino DM could provide strong clues for explaining neutrino mass and baryogenesis [22], such as the scenario advocated in the νMSM model [23–26].

Due to several sensitive x-ray instruments, such as Chandra, Suzaku, XMM-Newton, and INTEGRAL, stringent constraints on x-ray line emission have been obtained

*chun-yu.ng@weizmann.ac.il
†roachb@mit.edu
‡kmperez@mit.edu
§beacom.7@osu.edu
‖horiuchi@vt.edu
¶krivonos@iki.rssi.ru
**wik@astro.utah.edu

using many different observations (e.g., Refs. [27–33]). Interest in these topics was heightened with the tentative detection of a 3.5-keV line from cluster observations [34], which was followed up by many observational studies [35–56]. The nature of this line is still inconclusive. The line could be a signature of sterile neutrino DM [57] or other candidates [58–62]. However, as the line flux is weak, astrophysical modeling systematics [37,41] or new astrophysical processes [63,64] could also be the explanation. New detectors [44,56,65,66] or techniques, such as velocity spectroscopy [67,68], are likely required to fully determine its nature. (Recently, Ref. [69] claimed that blank-sky observations with XMM-Newton disfavor the DM interpretation of the 3.5-keV line. On the other hand, Ref. [70] claims detection of the 3.5-keV line in the Milky Way halo up to 35° with XMM-Newton, and refutes the claim of Ref. [69].)

For x-ray searches of DM, NuSTAR provides unique capabilities in the hard x-ray band, filling a sensitivity gap that persisted for many years [71] (partially covered by Fermi-GBM [72]). The first NuSTAR DM search was performed with focused observations of the Bullet Cluster [45]. But it was soon realized that by taking advantage of the open telescope design and using "0-bounce photons" (photons that enter the detector without passing through the reflecting optics), a larger (unfocused) field of view (FOV) can be achieved, thus boosting the sensitivity to the diffuse DM emission. Stringent constraints were then obtained using the extragalactic background [52] and Galactic Center observations [54]. Interestingly, a 3.5-keV line is also included in the NuSTAR instrumental background [73]. The background nature of this line has been questioned in Ref. [52]. However, Ref. [54] found evidence of the 3.5-keV line in Earth-occulted data, which suggests that the line has a detector background origin. The line is also close to the energy threshold of the detector; detailed studies of its possible instrumental origin are ongoing. Future work from the NuSTAR Collaboration is expected to elucidate the nature of this line in the NuSTAR data.

In this work, we search for DM lines with a combined 1.2 Ms of observations of M31, and offer several improvements on previous works. Compared to Ref. [54], the reduction of the astrophysical background, especially from astrophysical emission lines, improves the sensitivity to DM. We also consistently include both focused (2-bounce photons) and unfocused (0-bounce photons) FOV in signal modeling. To reduce potential systematic errors from stacking different datasets, we devise a method to statistically combine sensitivities from individual observations.

We present our NuSTAR data analysis in Sec. II, our DM signal modeling in Sec. III, and our DM results in Sec. IV. We conclude in Sec. V.

II. NuSTAR DATA ANALYSIS

In this section, we describe the NuSTAR instrument, the NuSTAR M31 observations, and details about the 0-bounce and 2-bounce FOV. We comment on the current difficulties in modeling the low-energy NuSTAR background. Lastly, we detail the modeling of the spectral data.

A. The NuSTAR instrument

As the first focusing hard x-ray observatory, NuSTAR provides a unique platform for studying astrophysical phenomena—including light DM candidates such as keV-scale sterile neutrinos. The NuSTAR design is detailed in Ref. [74], but we restate some relevant aspects here.

The NuSTAR science instrument consists of two independent, coaligned focal-plane modules (FPMs), with each FPM consisting of an x-ray optic and a detector. The energy resolution is set by the x-ray detectors, which have a FWHM of 0.4 keV for 5-keV photons, increasing to 0.9 keV for 70-keV photons. The x-ray optics are conical approximations of the grazing-incidence Wolter-I design, with nested Pt/C multilayer-coated mirrors. After entering the telescope, x rays reflect once off a parabolic mirror segment, followed by a hyperbolic mirror segment. These correctly focused x rays are called "2-bounce" photons, as they reflect twice inside the optics. NuSTAR is sensitive to 2-bounce photons with energies 3–79 keV. The lower limit is due to absorption by the dead layer of the CdZnTe detector, the Pt contact coating, and the 100-μm-thick Be window, effects which become significant only for $E <$ 10 keV [75]. The upper limit is set by the Pt K edge of the optics. Both FPMs have the same essentially overlapping $13' \times 13'$ FOV for 2-bounce photons.

The NuSTAR optical elements and detectors are separated by a 10-m mast, which is open to the sky. The observatory therefore includes a series of aperture stops to limit unfocused x rays from striking the detectors. However, this shielding is not complete, and there remains a circular region of radius $\sim 3.5°$ on the sky (partially blocked by the optics bench), from which x rays can strike the detectors without interacting with the optical elements. These are called 0-bounce photons. The energy range for these 0-bounce photons is not constrained by the performance of the optics, and thus extends up to the instrumental limit of 165 keV. Similar to the 2-bounce photons, 0-bounce photons are also subject to absorption effects from detector components at low energy.

B. NuSTAR's view of M31

To probe the diffuse x-ray emission from the direction of M31, we use both NuSTAR's 0-bounce photons from the wide-angle unfocused FOV and the 2-bounce photons from the narrower focused FOV. Unlike our previous work [54], none of the observations used in the present analysis were contaminated by significant "stray light" or "ghost rays" resulting from bright, isolated off-axis x-ray sources (the latter of which are sometimes referred to as "1-bounce" photons).

TABLE I. NuSTAR observations of M31 used in this analysis, with 0-bounce effective areas after data cleaning.

	Pointing (J2000)	Effective exposure[a]	Detector area A_{0b}[b]	Solid angle $\Delta\Omega_{0b}$[c]
NuSTAR obsID	RA, DEC (deg)	FPMA/B (ks)	FPMA/B (cm^2)	FPMA/B (deg^2)
50026002001	11.0826, 41.3762	95.4/94.5	11.76/11.77	4.44/4.51
50026002003	11.0821, 41.3688	82.4/82.2	11.85/11.80	4.45/4.55
50026003002	11.3306, 41.5763	106.3/105.4	11.24/11.10	4.40/4.41
50110002002	11.1122, 41.3753	31.6/31.9	12.38/12.29	4.56/4.55
50110002006	11.1047, 41.3758	36.9/36.8	12.22/12.15	4.55/4.52
50110003002	11.3425, 41.5610	87.9/87.4	11.33/11.20	4.52/4.52
50111002002	11.1285, 41.3694	82.4/82.4	11.78/11.81	4.46/4.51
50111003002	11.3704, 41.5913	102.0/102.2	11.22/11.16	4.55/4.38
Stacked[d]	···	624.9/622.8	11.59/11.54	4.48/4.48

[a]After `OPTIMIZED` SAA filtering and solar flare removal.
[b]After bad pixel removal and point source masking.
[c]Average solid angle of sky from which 0-bounce photons can be detected, after correcting for removal of bad pixels, point source masking, and efficiency due to vignetting effects.
[d]The A_{0b} and $\Delta\Omega_{0b}$ for the stacked spectra are the exposure-time-weighted averages of the values for the individual observations.

Table I shows the eight observations we select from > 1.6 Ms of NuSTAR pointed observations of M31 from 2015 to 2018. These selected observations are optimized to avoid the bright emission from the center of M31 and contamination from bright point sources. M31 is the closest large galaxy to our own Milky Way, at a distance ∼785 kpc [76,77]—close enough to resolve bright x-ray point sources. (Specifically, the NuSTAR's 18″ FWHM angular resolution for 2-bounce photons corresponds to ∼70 pc at the distance of M31.) We select NuSTAR observations that include at most one or two resolved x-ray sources in the 2-bounce FOV. We then remove from our analysis all detector pixels corresponding to a radius 60″ around CXO 004429.57 + 412135.1 and CXO 004527.34 + 413253.5, and 100″ around CXO 004545.57 + 413941.5 [78]. No other point sources with Chandra flux (0.35–8.0 keV) greater than $\sim 2 \times 10^{-13}$ erg cm^{-2} s^{-1} have been reported in the 2-bounce FOV for any of the observations listed in Table I. The remaining M31 emission from faint sources [79] is included in the spectral modeling.

Data reduction and analysis are performed with the NuSTAR's data analysis software pipeline, `NuSTARDAS v1.5.1`. To minimize the charged-particle background due to NuSTAR passing through the South Atlantic Anomaly (SAA), we use the flags `SAAMODE=OPTIMIZED` and `TENTACLE=YES`. We also inspect the (3–10)-keV light curves for each observation and remove any time intervals with an elevated low-energy count rate that could be indicative of solar flares. There were three such observations (50026002001, 50026002003, and 50111002002), from each of which 5–10 ks of data were removed. After all the data cleaning, the total exposure time for both FPMs that is used in this analysis is ∼1.2 Ms.

Figure 1 shows the combined 0-bounce and 2-bounce sky coverage of these observations. The 2-bounce FOV avoids the bright astrophysical x-ray emission from the central region of M31, but is still near the center of the DM density distribution. Similarly, the 0-bounce FOV avoids much of the astrophysical x-ray emission from the M31 disk, but is still within the DM halo. For reference, the ∼200-kpc virial radius of the M31 halo [80] corresponds to ∼15° on the sky.

C. Combining 0-bounce and 2-bounce observations

Unlike previous NuSTAR sterile neutrino searches, which considered 0-bounce [52,54] and 2-bounce [45] photons separately, the present analysis consistently incorporates both. Although the 2-bounce FOV for these M31 observations is over 2 orders of magnitude smaller than the corresponding 0-bounce FOV, including the 2-bounce photons increases the sensitivity of our search for two reasons. First, as the DM density increases toward the center of M31, the integrated DM densities over the 2-bounce FOV can be higher than that of the 0-bounce FOV. Second, the 2-bounce effective area is larger than the 0-bounce effective area, and is maximized for $E \sim 10$ keV, which is an especially interesting energy range for sterile neutrino DM search.

To take advantage of all available data, we extract spectra from the full detector planes. Our spectral model must then account for the instrumental background, as well as astrophysical emission observed in 2-bounce and 0-bounce modes. We account for these multiple spectral components by assigning custom response files for the 0-bounce and 2-bounce spectral model components with the corresponding effective area (cm^2) and effective solid angle (deg^2) factors.

The energy-dependent NuSTAR 2-bounce effective area $A_{2b}(E)$ is determined primarily by the optical elements, and is calculated by `NuSTARDAS` for each observation. The nominal effective area for each FPM for *point sources* peaks at ∼500 cm^2 at 10 keV [74].

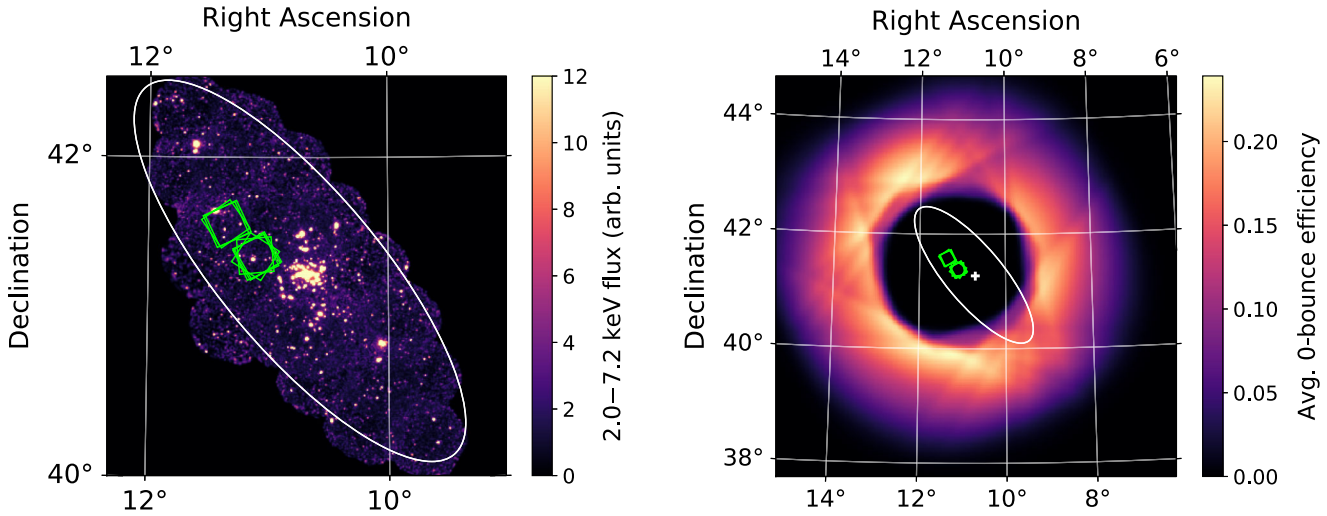

FIG. 1. Left: Magnified view of the M31 disk region. The green squares represent the 2-bounce FOV overlaid on the x-ray map by the XMM-Newton EPIC instrument [81,82], convolved with a Gaussian blur of radius 2 pixels. The color bar indicates the (2.0–7.2)-keV flux. The brightest x-ray sources in the FOV are removed in the analysis as described in Sec. II B. The white ellipse indicates the approximate optical size of the M31 disk. Right: An enlarged version of the left, with the color map indicating the averaged efficiency of the 0-bounce FOV for all observations (FPMA + B) listed in Table I. The average is weighted by each observation's exposure time after data cleaning and point source removal, and accounting for blocking by the optics bench and vignetting due to the aperture stops. The white cross indicates the center of M31.

For this analysis, the peak effective area is reduced to $\sim$100 cm^2 due to two reasons: First, the removed point sources are typically near the NuSTAR optical axis, where the effective area is the largest; second, the effect of vignetting as the spectra are extracted from the entire FPM as an extended source, where A_{2b} is averaged over the 2-bounce FOV. The 2-bounce solid angle $\Delta\Omega_{2b}$ is also slightly reduced from $13' \times 13'$ (0.047 deg^2) to $\sim$0.045 deg^2 for each FPM following point source removal. When fitting the 2-bounce components in the spectrum, we use the combined 2-bounce response $A_{2b}(E) \times \Delta\Omega_{2b}$, where the $A_{2b}(E)$ produced from `NuSTARDAS` already includes the Be window and the detector absorption effects.

The effective area A_{0b} for 0-bounce photons is set by the physical $\sim$15 cm^2 area of each detector, and is reduced to $\sim$11.5–12.5 cm^2 per detector after removing point sources. This is balanced, however, by an increased FOV compared to 2-bounce photons. Using the geometric model of NuSTAR in the `nuskybgd` code [73], we calculate the average solid angle $\Delta\Omega_{0b}$ from which 0-bounce photons can strike the detectors, including the effects of obscuration and vignetting introduced by the optics bench and aperture stop. Following data cleaning and point source removal, each FPM subtends an average solid angle $\Delta\Omega_{0b} \sim 4.5$ deg^2, almost 2 orders of magnitude larger than $\Delta\Omega_{2b}$. (These parameters are listed in Table I.) For 0-bounce spectral components, we use the combined 0-bounce response $\mathcal{E}_{Be}(E) \times A_{0b} \times \Delta\Omega_{0b}$, with the detector absorption effects included during spectral modeling. Additionally, the use of 0-bounce photons means that we are not limited to the (3–79)-keV energy range set by the NuSTAR optics; rather, we can extend our high-energy range up to $E = 100$ keV. Above that, we expect our instrumental background model to be less robust for line searches.

D. NuSTAR at low energy and the 3.5-keV line

Previous analyses have noted the presence of a line in the NuSTAR spectrum near 3.5 keV [52,73]. These works differ, however, in whether this line is attributable to an astrophysical (including DM) or instrumental origin. As the NuSTAR instrumental background is poorly understood below 5 keV, we do not include this energy range in our analysis. Instead, we comment here on the difficulties encountered when using this low-energy NuSTAR data and the foreseen avenues for future progress.

We investigate our instrumental background components using occulted data collected during the same M31 observation periods we use for our main analysis but when the NuSTAR FOV is blocked by Earth. We consider two spectral models for this data: the default NuSTAR instrumental background model and an "internal power-law" version of this model; the latter is motivated by fits to the occulted data themselves.

The default NuSTAR instrumental background model, as detailed in Sec. II E and Ref. [73], is derived from phenomenological fits to "blank-sky" observations. It is dominated at low energies by a 3.5-keV line, a 4.5-keV line, and an $\sim$1-keV thermal plasma component (the `apec` model in `XSPEC`) that is possibly attributed to reflected solar x rays. At high energies, it is dominated by a relatively flat continuum and a series of Lorentzian lines. We find that for energies above $\sim$20 keV, the occulted data are well

described by this model. Below ∼20 keV, however, the occulted data indicate residual emission remains that is not accounted for by this default model.

These low-energy occulted fits are improved if we modify the default model by replacing the ∼1-keV thermal plasma component with a power-law continuum. In this "internal power-law" model, we use occulted data to derive a best-fit power-law index and relative normalization with respect to the high-energy continuum; we then freeze both of these parameters in the instrumental background model applied to nonocculted data. This procedure has been validated on extragalactic observations, where it yields the correct expected spectral shape and flux for the cosmic x-ray background (CXB) [83,84].

To associate any detected line with an astrophysical, as opposed to instrumental, origin, the observed line flux should be smaller or nonexistent in the occulted dataset. Using the default instrumental background model, the 3.5- and 4.5-keV lines are each observed with comparable 90% C.L. line fluxes between occulted and nonocculted data. When we adopt the internal power-law background model to M31 data, the 3.5- and 4.5-keV line fluxes are again each observed with comparable 90% C.L. line fluxes between occulted and nonocculted data. However, the best-fit line fluxes differ between the default and power-law instrumental background models, between different observations of similar sky regions, and between FPMA and FPMB of the same observation. In addition, the fit is unstable when using the internal power-law model below 5 keV, where the 3.5- and 4.5-keV line strengths are found to be somewhat degenerate with the power-law index and normalization. This study reinforces the notion that these lines are backgrounds, though the statistics of the occulted sample is relatively limited. As a result, further interpretation, such as searching for any possible excess in low-energy line flux in the nonocculted M31 data, is difficult.

Due to these issues, we limit our analysis to $E \geq 5$ keV, or sterile neutrino DM mass $\geq$10 keV. This allows for a stable spectral fit and robust determination of line-flux limits. We see no difference in the $E \geq 5$ keV results between using the default or power-law internal background model. We use the default background model for the rest of the paper. We further note that the choice of the background model does not affect the $E < 5$ keV limits derived from the previous NuSTAR Galactic Center analysis [54]; this constraint was conservative, allowing the DM line to assume the full strength of any line in the data.

Detailed investigations of the NuSTAR instrumental background are beyond the scope of this paper. Work is ongoing now to exploit the full NuSTAR archival dataset to better constrain the origin and description of the instrumental background. Future NuSTAR analyses will be able to use this improved model to better constrain, or detect, low-energy line emission.

E. Spectral fit

We consider the NuSTAR data between 5 and 100 keV, as discussed above. We first fit each observation individually with their own set of parameters. In Sec. IV B below, we combine the fits to derive our primary results. Our spectral model consists of four components: the default NuSTAR instrumental background [73], 0-bounce and 2-bounce CXB components, and a 2-bounce component from the diffuse M31 emission. The first component does not depend significantly on the FOV of the observations, while the rest do. Note that we use both 0-bounce and 2-bounce astrophysical components normalized as described in Sec. II C.

Because the number of photons is large, we are able to choose a binning scheme that is sufficiently fine to identify any narrow spectral features, while also minimizing the statistical error in each bin. We adopt a logarithmic binning scheme of 100 bins per decade in energy for the ∼30-ks observations (50110002002 and 50110002006), and 200 bins per decade for the remaining, longer observations. These binning schemes provide a statistical uncertainty that is everywhere ∼10% per bin. We note that the binning is always narrower than the NuSTAR energy resolution (FWHM) for photon energies 5–20 keV, which is the most interesting energy range for sterile neutrino DM searches.

We adopt the default NuSTAR background model of Wik *et al.* [73], including internal detector backgrounds, a solar component, and the CXB. The NuSTAR internal background is modeled by a broken power-law continuum with a break at 124 keV, as well as a complex of Lorentzian activation and fluorescence lines, which together comprise much of the background above 20 keV. The continuum power-law index, as well as the line energies and widths, are fixed, while the normalizations of these components are free to fit independently for all observations and for FPMA and FPMB. This is due to different detector backgrounds and sky regions between observations and FPMs. As described in Sec. II D, we also include an ∼1-keV diffuse thermal plasma component with emission lines believed to result from solar activity. This is the source of the lines near 6.5 and 8 keV. The CXB resulting from unresolved extragalactic emission is described by a cutoff power law with spectral indices, cutoff energy, and flux fixed to the values measured by INTEGRAL [84].

Observations from ROSAT [85], XMM-Newton, and Chandra [86] reveal a diffuse x-ray component within the disk of M31, thought to result from a population of unresolved point sources. We adopt a single power-law model for the energy spectrum of 2-bounce photons from these unresolved M31 sources, with normalization and spectral index free to fit. We obtain 2-bounce M31 spectral indices in the range ∼1.3–1.7 for the observations in this analysis, consistent with the population of faint x-ray sources in, e.g., Ref. [79]. Since the NuSTAR optics bench blocks the disk of M31, as shown in Fig. 1, there is no need

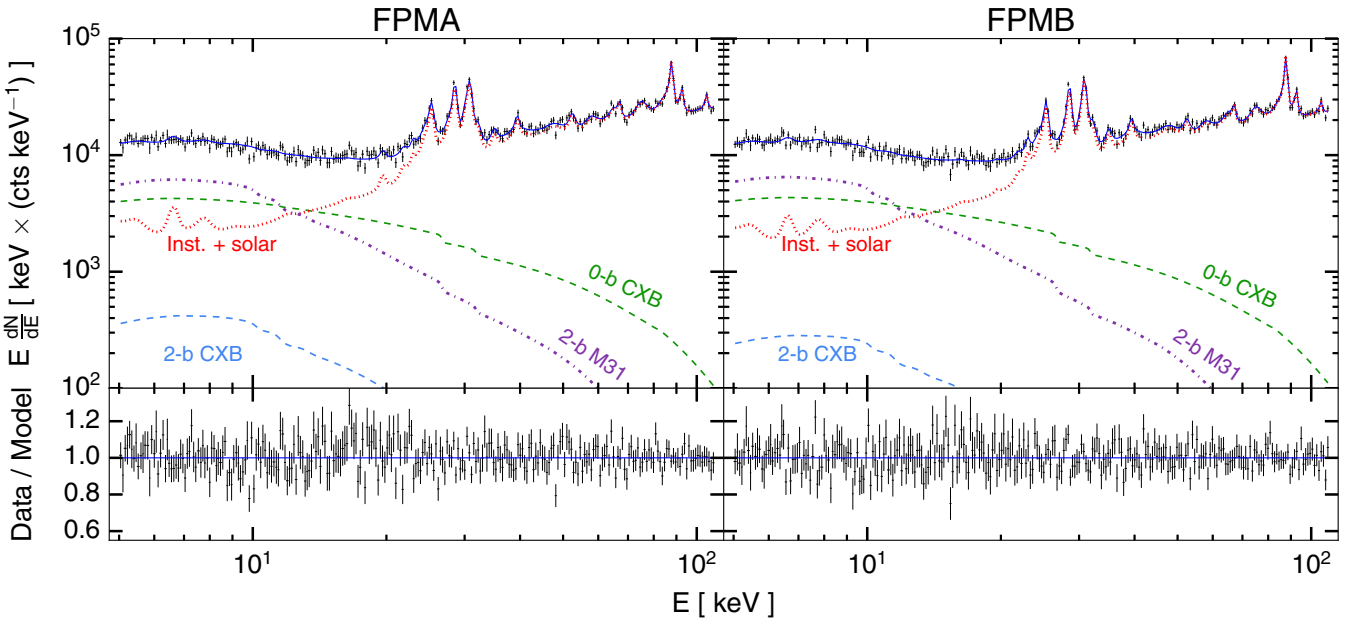

FIG. 2. Data and model spectra from FPMA (left) and FPMB (right) for the example of obsID 50026002003, including contributions from 0-bounce CXB, 2-bounce CXB, 2-bounce M31, and instrumental/solar background. The 0-bounce M31 component is not included, as the M31 disk is blocked in the 0-bounce FOV. See Sec. II E for details. The lower panels show the ratio of the data to the best-fit model. All error bars indicate 1σ statistical uncertainties, with reduced χ^2 of 1.15 and 0.99 for FPMA and FPMB, respectively. The differing contributions for the 2-bounce CXB component between FPMA/B arise primarily from differences in the position of the masked point source with respect to the optical axis, as discussed in Sec. II C. Results for other observations are similar.

to include a diffuse 0-bounce M31 component. There is also evidence for at least one thermal plasma component with 0.1 keV $\lesssim kT \lesssim$ 0.7 keV to the diffuse M31 x-ray background [87], though such a low-temperature component would not be visible to NuSTAR in the energy range of this analysis. We stress that a conclusive identification of the diffuse M31 x-ray background is not necessary for the present analysis; rather, it is the use of a physically motivated model that provides a good fit to the data that is most important.

All noninstrumental components, including astrophysical, DM, and the solar background components, are subject to absorption by materials on the surface of the NuSTAR detectors. This includes absorption from the ∼0.11-μm Pt contact coatings, as well as the ∼0.27-μm layer of inactive CdZnTe on the detector surfaces. Combined, these components cause an ∼25% absorption for 5-keV photons, decreasing to ∼5% for 10-keV photons. (We note the effect of the Be shield is already included in the effective area.)

The astrophysical components are also subject to absorption from the interstellar medium. For the 2-bounce CXB and 2-bounce M31, the absorption is calculated using the `tbabs` model in `XSPEC`, which incorporates the abundances given in Ref. [88] and the photoionization and absorption cross sections given in Refs. [89,90]. The equivalent neutral hydrogen column density $N_{\rm H}$ toward the disk of M31, near the 2-bounce FOV of the observations in this analysis, is $\sim 5 \times 10^{21}$ cm^{-2} [91]. The corresponding optical depth is $\tau \sim 0.03$ for 1-keV photons [92], and decreases with energy. The $N_{\rm H}$ value for 2-bounce observations is fixed during spectral modeling.

Similarly, for the 0-bounce CXB, we apply a fixed $N_{\rm H}$ value of $\sim 7 \times 10^{20}$ cm^{-2}, as observed in the direction of M31 without the disk [93,94]. As the 0-bounce $N_{\rm H}$ value is almost an order of magnitude lower than the 2-bounce $N_{\rm H}$ value, absorption is negligible; we include it for completeness.

For DM lines, as most of the signal comes the 0-bounce observations (see Sec. III), only absorption from detector materials is relevant. This is at most an ∼25% effect at 5 keV; we include it to be conservative and consistent.

Figure 2 shows the spectrum for obsID 50026002003 and the corresponding spectral fit components, as an example. The vertical-axis units on this figure reflect proportional differences in the number of counts N in each bin, to wit:

$$E\frac{dN}{dE} = \frac{dN}{d(\ln E)} \simeq \frac{dN}{d(2.3\log_{10}E)}.$$

As the bins are evenly spaced in $\log_{10} E$, with 200 bins per decade in the example spectra, each bin has a width 0.005 in $\log_{10} E$. The number of counts in the bin with $E \sim 10$ keV, e.g., is

$$1.2 \times 10^4 \text{ keV} \times (\text{counts keV}^{-1}) \times \frac{2.3}{200} \approx 130 \text{ counts},$$

corresponding to an ∼10% statistical uncertainty per bin. The fit has reduced χ^2 of 1.15 and 0.99 over 239 degrees of freedom for FPMA and FPMB, respectively. We find similar results for all other observations. Thus, we conclude that the fits are acceptable for the individual observations. In Sec. IV, we discuss details of the fit residuals as well as the procedure for combining observations. While the astrophysical components dominate below ∼13 keV, both the astrophysical continuum and line emission are much lower compared to our previous Galactic Center analysis [54]. This enhances the DM sensitivity, particularly in the mass range ∼12–20 keV, where previously the search was limited by strong Fe line emission from the Galactic Ridge x-ray excess.

III. DARK MATTER SIGNAL MODELING

In this section, we describe the modeling of DM event rates in the NuSTAR observations.

A. DM distributions

To search for DM lines in the NuSTAR observations, we need to compute the expected DM event rate taking into account both the 0-bounce and 2-bounce FOV. Also, DM from the Milky Way (MW) and M31 halo can both appreciably contribute to the signal.

The expected photon line intensity (differential flux per solid angle) from sterile neutrino DM decay is

$$\mathcal{I} \equiv \frac{dF}{dEd\Omega} = \frac{\Gamma}{4\pi m_\chi}\int d\ell(\rho_{\rm MW}+\rho_{\rm M31})\frac{dN}{dE}, \quad (1)$$

where Γ is the DM decay rate, m_χ is the DM mass, ρ is the DM density distribution for the MW or M31, ℓ is the line-of-sight distance that we integrate over, and $dN/dE = \delta(E - m_\chi/2)$ is the sterile neutrino DM decay spectrum with the line energy being half of the DM mass. The line width is narrow compared to the NuSTAR energy resolution; thus a delta function approximation is appropriate.

To evaluate the line-of-sight integrals for the MW we use the sNFW profile from Ref. [54], which was motivated by simulations and MW kinematic data [95] (see Ref. [54] for details). For the M31 halo, we use the NFW profile from Ref. [80], where the mass distribution was inferred from a multitude of imaging and kinematic data. The scale density, scale radius, and the virial radius are $\rho_s = 0.418$ GeV/cm^3, $r_s = 16.5$ kpc, and $R_{200} = 207$ kpc, respectively. In the next section, we discuss the impact of the choice of density profiles to the DM sensitivity.

We neglect the cosmological decaying DM contribution to the extragalactic background. The spectrum of this signal is broadened by cosmological redshifts, and the flux is negligible compared to the other components that we consider [54].

B. DM event rate in NuSTAR

The number of DM signal photons, $N_{\rm DM}$, that would be detected by NuSTAR is the DM intensity [Eq. (1)] integrated over the line spectrum and convolved with the detector response for that particular observation. It is

$$N_{\rm DM} = \sum_{j=0{\rm b},2{\rm b}} A_j T_{\rm obs}\int_{\rm FOV}\xi_j \mathcal{I} d\Omega = \frac{\Gamma}{4\pi m_\chi} T_{\rm obs}(A_{0{\rm b}}\Delta\Omega_{0{\rm b}}\mathcal{J}_{0{\rm b}} + A_{2{\rm b}}\Delta\Omega_{2{\rm b}}\mathcal{J}_{2{\rm b}}), \quad (2)$$

where $A_{0{\rm b},2{\rm b}}$ are the effective areas for 0-bounce and 2-bounce observations, $T_{\rm obs}$ is the observing time, and $\xi_{0{\rm b},2{\rm b}}$ are the pixel efficiencies of the FOV that takes into account, e.g., the optics bench blocking, and $\Delta\Omega = \int_{\rm FOV}\xi d\Omega$ is the effective FOV. We also define the FOV-dependent J-factor,

$$\mathcal{J} = \frac{1}{\Delta\Omega}\int d\Omega\,\xi\int d\ell(\rho_{\rm MW}+\rho_{\rm M31}) \quad (3)$$

for both 0-bounce and 2-bounce observations.

For the 0-bounce FOV, as shown in Fig. 1, there is not much variation in $\mathcal{J}_{0b}$ among different observations, given that they basically all point in the same direction. The MW halo also has a larger contribution to the J-factor compared to the M31 halo. This is because the bulk of the M31 center is blocked by the mirror module, so only the outskirts of the M31 contribute to the J-factor. Roughly, the MW part of the $\mathcal{J}_{0b}$ is about 1.5 to 2.3 times larger than that of M31. For the 2-bounce FOV, the situation is reversed, as it points closer to the center of M31. Roughly, the M31 part of $\mathcal{J}_{2b}$ is about 2.1 to 3.4 times larger than that of the MW.

Unlike previous works, where either the 0-bounce [45] or the 2-bounce contribution is neglected [52,54], we include both in this work. To see how much the 2-bounce FOV affects the result, we consider the "enhancement factor,"

$$\left(1+\frac{A_{2{\rm b}}(E)\Delta\Omega_{2{\rm b}}\mathcal{J}_{2{\rm b}}}{A_{0{\rm b}}\Delta\Omega_{0{\rm b}}\mathcal{J}_{0{\rm b}}}\right), \quad (4)$$

which represents the signal enhancement due to the 2-bounce FOV. The enhancement factor is energy dependent due to the 2-bounce effective area $A_{2{\rm b}}(E)$.

Figure 3 shows the enhancement factors for all the considered observations. They peak around 10 keV and can be as high as 1.4. The enhancement from the 2-bounce contribution is negatively impacted by the point source removal and vignetting effects as described in Sec. II C, which significantly reduced the effective area.

After combining the observations (see Sec. IV B), at ∼10 keV photon energy, the 0-bounce MW, 0-bounce M31,

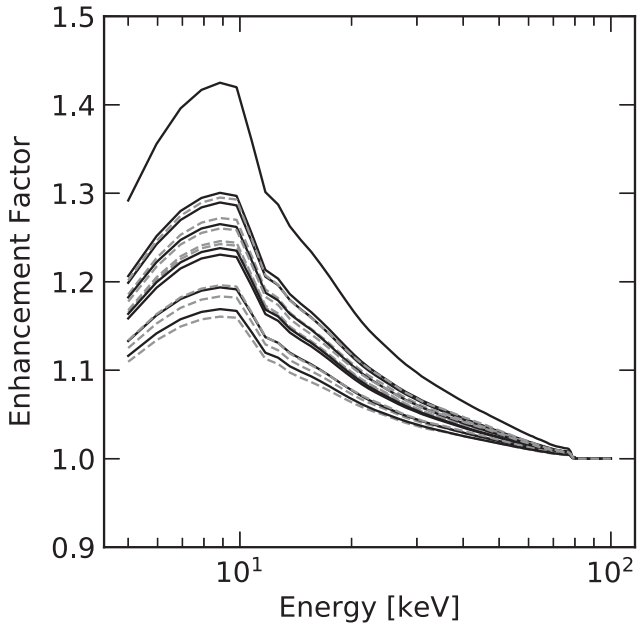

FIG. 3. Enhancement due to the inclusion of the 2-bounce FOV relative to the 0-bounce FOV for all observations across FPMA (solid) and FPMB (dashed) considered in this work. The energy dependence comes from the effective areas of the 2-bounce FOV.

2-bounce MW, and 2-bounce M31 components contribute about 50%, 30%, 5%, and 15% of the signal, respectively.

IV. DARK MATTER LINE SEARCH

In this section, we describe the line analysis for each individual M31 observation, then the combined analysis. Finally, we present our results for sterile neutrino DM.

A. NuSTAR observation line analysis

For each M31 observation and FPM, we search for potential DM line signals by scanning in the (5–100)-keV energy range, with 100 logarithmically spaced steps per decade in energy. In this scheme, near $E = 5$ keV, the steps are ∼0.1 keV apart, growing to ∼2 keV apart by $E = 100$ keV. This is to be compared to the detector energy resolution of 0.4 keV for 5-keV photons and 0.9 keV for 60-keV photons. Thus, any new line present with $E \lesssim 40$ keV will be several steps wide. We observe no significant change in results if we use a finer sampling scheme, e.g., 200 steps per decade. For each scanned line energy, we add a hypothetical DM line component to the model and take into account all detector response and absorption effects (see Sec. II C). As the line width is dominated by the detector resolution, the DM line component has only one free parameter—the normalization—for each scan, which we parametrize with the DM decay rate Γ using Eq. (2).

We define the function $\chi^2(\Gamma)$, which is the best-fit chi-squared value of the fit to the data after adding the DM signal line to the model at a specific value of Γ. We find the $\chi^2(\Gamma)$ distribution for each scanned line energy. It is important to note that for every value of Γ, $\chi^2(\Gamma)$ is minimized with respect to all free spectral model parameters. Thus, when scanning at a known background line (detector or astrophysical) energy, $\chi^2(\Gamma)$ would be at the minimum value for Γ smaller or equal to the corresponding background line strength. In other words, when setting the limit at the presence of a background line, we conservatively allow the DM line flux to be at least as large as the background line feature.

B. Combined analysis with all M31 observations

Having obtained the $\chi^2(\Gamma)$ distributions for all observations, we now combine them to take advantage of the full statistical power of the 1.2 Ms of NuSTAR M31 data. We consider the object X^2, which is the sum of all the individual χ^2 distributions,

$$X^2(\Gamma) = \sum_{\text{obs}} \chi^2(\Gamma). \tag{5}$$

In the case of a detection or in the presence of a background line feature, $X^2(\Gamma)$ would reach a minimum at a particular Γ_0 value, with the line significance given by $\sqrt{X^2(\Gamma = 0) - X^2(\Gamma_0)}$. In the case of a null detection, the minimum would be at $\Gamma_0 = 0$. In all cases, we can obtain the 95% one-sided upper limit by finding Γ_{95} such that $X^2(\Gamma_{95}) = X^2(\Gamma_0) + 2.71$.

Given that individual observations are minimized independently, they are allowed to have their own set of background parameters. This is an improvement over previous stacked analyses [52,54], which used a single background model to describe the sum of many observations. Our new approach avoids producing artificial spectral features due to the stacking of potentially different continuum backgrounds in each observation. In fact, it is known that the background parameters are slightly different between the two FPMs. The new approach also effectively increases the number of d.o.f., which alleviates the need for adding an extra systematic error factor to improve the fit, as in our previous Galactic Center analysis [54]. In the future, this approach can even be used to combine the sensitivities from observations of different targets. In Appendix A, we detail the procedures of the stacked analysis. The results are found to be consistent with our default analysis.

In the line search, we identify several energy regions where the fit noticeably improves when a DM line is added. These are at photon energies around 5–6, 15–16, 28, and 80 keV. For the 5–6-keV region, the residual is located at the edge of our selected data. As mentioned in Sec. II D, the low-energy NuSTAR background model is quite uncertain. In particular, it is likely that the actual solar component differs from that in the default background model, due to the Sun being a variable source. In contrast to our previous Galactic Center analysis [54], this problem in the

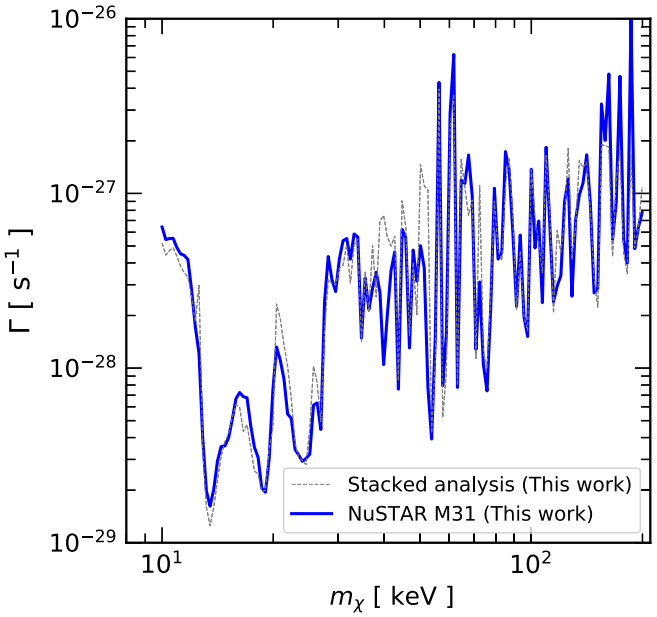

FIG. 4. Derived upper limit on DM decay rates from combined NuSTAR M31 observations. Results from the default analysis are shown with a blue line, and that from the stacked analysis (see Appendix A) are shown with a gray dashed line. We have assumed each DM decay produces one monoenergetic photon with energy half the DM mass.

instrumental background is highlighted by the low astrophysical flux in the data. For 15–16 keV, it is known that the current background model has difficulty in fitting the data here, likely due to this being the transition region between the astrophysical and instrumental continuum backgrounds. A similar residual was also identified in our previous Galactic Center analysis [54]. For the 28- and 80-keV regions, these are where the data are dominated by strong and complicated detector activation and fluorescence lines, as shown in Fig. 2, thus making the astrophysical interpretation difficult and unlikely. We also note that the corresponding line fluxes at 28 and 80 keV are already being constrained by INTEGRAL [29,30]. As a result, we do not interpret all these residuals as having an astrophysical origin. The corresponding DM limit is set conservatively, with the DM flux allowed to saturate the full residual, thus resulting in worsened sensitivities in these regions.

Overall, we see no obvious candidates of a DM signal. We thus proceed to derive upper limits for the DM decay rate, following the procedure described above.

Figure 4 shows the derived constraints on the decay rate, Γ. In the energies mentioned above, where we see positive residuals, our limit is weakened. In other energies, where there are background lines, our limit is also weakened, causing many "spikes" in the limit. For comparison, we also show the results from the stacked analysis, which are consistent with the default analysis.

Our results are robust with respect to the choice of DM density profiles. Because M31 is located relatively far away from the Galactic Center in celestial coordinates ($\sim$120°), the MW part of the signal is insensitive to the choice of the MW profiles. Using different profiles considered in Ref. [54] only changes the expected MW signal by $\sim$10%, in contrast to the potential large uncertainties when using the Galactic Center [96]. For the M31 part, because the signal is dominated by the 0-bounce observations, which are only sensitive to the outskirts of the M31 halo ($\gtrsim$10 kpc), using different halo profiles considered in Ref. [42] changes the total sensitivity by only $\lesssim$5%.

While we focus on sterile neutrino DM, the limit on the sterile neutrino DM decay rate can be easily translated and applied to other decaying DM models. In Appendix B, we also derive constraints on the cross section for annihilating DM models.

C. Constraints on sterile neutrino DM

We now consider the implications of our result for sterile neutrino DM, one of the prime candidates for decaying DM in the x-ray band.

1. X-ray constraints

Sterile neutrino DM, regardless of the production mechanism, decays radiatively ($\chi \to \gamma + \nu$) via the mixing with active neutrinos, with a rate [8,9]

$$\Gamma = 1.38 \times 10^{-32}\ \mathrm{s}^{-1} \left(\frac{\sin^2 2\theta}{10^{-10}}\right) \left(\frac{m_\chi}{\mathrm{keV}}\right)^5, \qquad (6)$$

where θ is the mixing angle with active neutrinos. Thus, x-ray observations can be used to place model-independent upper limits on the mixing angle [10,11], which is the main goal of this work.

Figure 5 shows the mass-mixing angle parameter space plane. Our constraint from the combined M31 observations converted from decay rates using Eq. (6) is shown by the blue line. For comparison, we also show constraints from many previous x-ray searches detailed in Ref. [54]. Compared to our previous Galactic Center analysis [54], our present results benefit from the absence of strong astrophysical line emission around 6.7 keV. Compared to the deep sky analysis [52], our present analysis, despite having less exposure, benefits from the inclusion of the DM contribution from the M31 halo, as well as from an improved analysis procedure that minimizes systematic effects from stacking spectra. Overall, our new results improve the constraints for DM masses between 12 and 20 keV.

2. A finite window in the parameter space

If sterile neutrino DM is produced via mixing in the early Universe, then additional constraints from DM production and warm DM considerations also apply. These constraints,

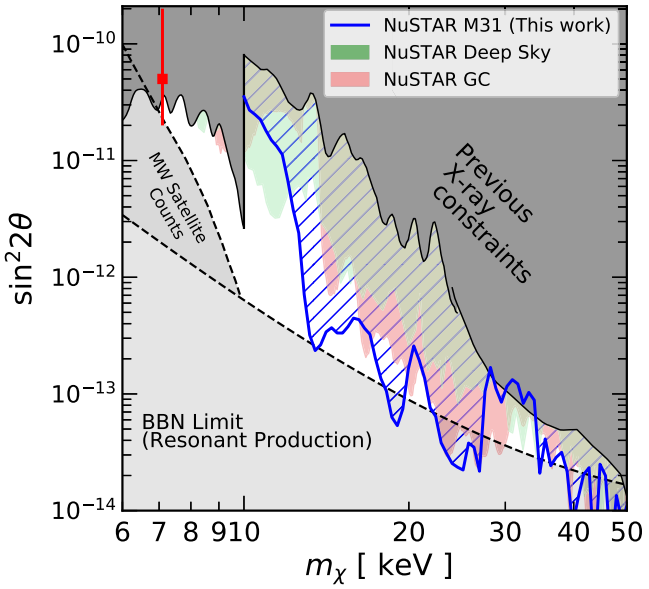

FIG. 5. The mixing angle-mass parameter space for sterile neutrino DM. Our limit obtained from the combined M31 observations is shown by the blue line and the hatched region. For comparison, we also show NuSTAR constraints from deep sky [52] and Galactic Center [54] observations. The previous x-ray constraints are shown in the dark gray region (see Ref. [54] for details). For sterile neutrino DM produced via mixing, the light gray constraints from satellite-counts [97] and BBN constraints on lepton asymmetry also apply. In this case, a finite allowed window remains, shown in white. The red point indicates the claimed 3.5-keV line detection.

together with the x-ray constraints, form a window in the parameter space that is bounded on all sides.

Sterile neutrino DM can be naturally produced via neutrino mixing with active neutrinos, either nonresonantly 12]] or resonantly [13]. Nonresonant production defines a line in the parameter space of mass and mixing angle, and is already in strong tension with exiting constraints. Resonant production can occur if there was primordial lepton asymmetry, which allows sufficient DM to be produced with a range of smaller mixing angles than nonresonant production. However, big bang nucleosynthesis (BBN) places an upper limit on the lepton asymmetry at that epoch [98–100]; the limit on the asymmetry is often expressed through the dimensionless parameter $L_6 \leq 2500$. Using the latest sterile neutrino DM production code `sterile-dm` [101], we find the corresponding *lower* bound on the mixing angle; below that neutrino mixing is unable to produce enough DM to match the observed abundance. We note that our result is consistent with that found in Ref. [97]. For specific models such as νMSM, the production constraint is typically more stringent than the BBN bound (a higher lower bound on the mixing angle). For generality and to be conservative, we only consider the BBN bound.

Sterile neutrino DM produced via mixing can also be a warm DM candidate. While warm DM could be a potential solution to address some small-scale problems of cold DM cosmology [102–104], astrophysical observations such as satellite counts or Ly-α forests also constrain DM from being too warm [97,105,106], which puts comparable mixing angle-dependent lower limits on the DM mass that are stronger than the more robust model-independent phase-space constraints [33,107]. We thus only consider the satellite-counts constraints from Ref. [97].

Figure 5 also shows the production and warm DM constraints. In the context of sterile neutrino DM produced via neutrino mixing, our M31 x-ray constraint reduces the previously available parameter space by close to one-third.

V. CONCLUSIONS AND OUTLOOK

We search for x-ray lines from sterile neutrino DM decay using 1.2 Ms of combined NuSTAR M31 observations. We consistently include the focused (2-bounce) FOV, which enhances the sensitivity compared to previous works that considered only the unfocused (0-bounce) FOV. We also opt to statistically combine the sensitivities of individual observations. Compared to a usual stacking analysis, this reduces the potential systematic error from stacking spectra with different underlying continuum spectra.

We see no evidence of DM signals, and thus report upper limits for photon line energies 5–100 keV, or sterile neutrino DM masses 10–200 keV. Specifically, the constraints are improved the most in the mass range ~12–20 keV. For more general DM candidates, we also report limits in decay rate and annihilation cross section. For sterile neutrino DM produced via mixing, we reduce the available parameter space by close to one-third.

We demonstrate that adding the 2-bounce component can meaningfully enhance the DM sensitivity, up to a factor of 1.4. However, in this work the enhancement is not optimal, as the center part of the 2-bounce FOV is removed due to the presence of point sources. In the future, for other observations where such cuts are not needed, the 2-bounce contribution can be increased by a factor ~2. The 2-bounce contribution could also be higher if the FOV is pointed at regions with more concentrated DM distribution.

Our statistical analysis approach in this work is mainly aimed to reduce systematic errors from the stacking process. However, in principle, it can also be used to combine completely different observations, such as Galactic Center and M31, after they are properly modeled. This will further enhance the DM search sensitivity.

In the future, especially with an improved understanding of the low-energy NuSTAR instrumental background model, we anticipate NuSTAR will be a powerful tool to test the remaining parameter space window shown in Fig. 5, and perhaps also test the tentative 3.5-keV line signal. Ruling out this window would mean that sterile neutrino DM cannot be simply produced via neutrino mixing. However, we stress that this would not rule out generic sterile neutrinos as a DM candidate. Nevertheless, this

would rule out the νMSM model [23–26], which was proposed to simultaneously explain the nature of DM, baryogenesis, and the origin of neutrino mass.

ACKNOWLEDGMENTS

The computational aspects of this work made extensive use of the following packages: SAOImage DS9 distributed by the Smithsonian Astrophysical Observatory, the SciPy ecosystem [108], particularly Matplotlib and NumPy, and Astropy, a community-developed core PYTHON package for astronomy [109,110]. This research has made use of data and/or software provided by the High Energy Astrophysics Science Archive Research Center, which is a service of the Astrophysics Science Division at NASA/GSFC and the High Energy Astrophysics Division of the Smithsonian Astrophysical Observatory. Portions of this work include observations obtained with the NuSTAR mission, a project led by the California Institute of Technology, managed by JPL, and funded by NASA, as well as XMM-Newton, an ESA science mission with instruments and contributions directly funded by ESA Member States and NASA. We thank Shuo Zhang for helpful comments and discussions. K. C. Y. N. is supported by a Croucher Fellowship and a Benoziyo Fellowship. B. M. R. receives support from the MIT Department of Physics and Dean of Science Fellowships. K. P. receives support from the Alfred P. Sloan Founation. J. F. B. is supported by NSF Grant No. PHY-1714479. S. H. is supported by the U.S. Department of Energy under Award No. DE-SC0018327. R. K. acknowledges support from the Russian Science Foundation (Grant No. 19-12-00396).

APPENDIX A: STACKED ANALYSIS

As described in Sec. IV, to derive a constraint on a potential DM line flux, we fit each observation separately, and statistically combine the flux constraints for each observation to produce the results shown in Fig. 5. This approach allows us to model the background for each observation separately, reducing the systematic effects of combining backgrounds, which may vary for each observation. As a cross-check, we also follow our previous approach in analyzing Galactic Center data [54], i.e., stacking the individual spectra from each observation and deriving DM limits from the stacked spectra. In this Appendix, we discuss the results derived from stacking the spectra, and show that they are consistent with the statistical-combination approach used in Sec. IV.

We use the addascaspec tool to stack the spectra for FPMA/B separately, as each FPM has slightly different instrument responses and internal backgrounds. The 0-bounce and 2-bounce effective areas (cm^2) and solid angles (deg^2) for the stacked spectra are taken to be the exposure-time-weighted averages of the values from the individual observations. The best-fit reduced χ^2 for the stacked spectra, in the null DM hypothesis, is ~2.6 for each FPM (239 d.o.f. each, for 200 logarithmically spaced energy bins per decade), significantly worse than that of the individual observations. As the statistical errors are small ($\lesssim$5%), systematic effects dominate. In particular, we find large positive residuals for $E < 6$ keV and ~15–30 keV, similar to those identified in Sec. IV B using the statistical-combination approach. This reinforces the point that the instrumental background model is not sufficient to describe these regions, and the fit cannot be improved via better analysis procedures. Additionally, we find that the derived 2-bounce M31 flux, relative to the (fixed) CXB components, is consistent between the statistical-combination and stacked approaches, as is the derived 2-bounce M31 power-law index. We then use the same line-search procedure on the stacked spectra as was described in Sec. IV B to derive 95% one-sided upper limits on any DM flux (in the case of a null detection) or to find potential DM signals. We find linelike signals in the same energy ranges as were obtained using the statistical-combination method, though as was discussed previously, a DM interpretation for these features is implausible.

Overall, we find that our statistical-combination and stacking approaches provide constraints in the mass-mixing angle plane that are consistent at the ~10% level, as shown in Fig. 4. This supports our use of the statistical-combination procedure to derive DM limits, as it provides a better fit (i.e., improved χ^2/d.o.f.) to the data without the inclusion of an overall systematic uncertainty, which weakened our previous limit [54]. Additionally, the statistical-combination procedure will allow us to combine

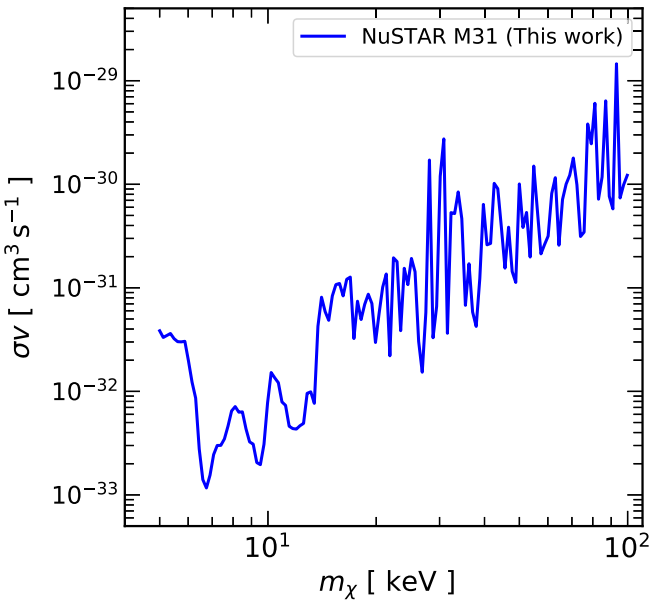

FIG. 6. Upper limit on DM annihilation cross sections from combined NuSTAR M31 observations. We have assumed each DM annihilation produces two monoenergetic photons with energy equal to the DM mass.

constraints from different regions on the sky in future analyses, as we can independently model the backgrounds in each region.

APPENDIX B: CONSTRAINTS ON DM ANNIHILATION

In this section, we derive upper limits on the DM annihilation cross section. While thermally produced s-wave WIMPs that couple to the visible sector are strongly constrained at the keV scale (see discussion in Ref. [111]), DM with nonstandard thermal history could still produce x-ray lines through annihilation (e.g., see Refs. [60,61]). To find the limit on the annihilation cross section, we consider the case of $\chi\chi \to \gamma\gamma$, and write the analog of Eq. (1),

$$\mathcal{I} = \frac{\sigma v}{8\pi m_\chi^2} \int d\ell (\rho_{\rm MW}^2 + \rho_{\rm M31}^2) \frac{dN}{dE}, \tag{B1}$$

where σv is taken to be the velocity-independent annihilation cross section, and the spectrum is $dN/dE = 2\delta(E - m_\chi)$. Then it is straightforward to compute the annihilation version of the J-factors and repeat the analysis to obtain the upper limit. We conservatively neglect the potential J-factor enhancement due to DM substructures (see, e.g., Refs. [112,113]).

Figure 6 shows our derived upper limit on the annihilation cross section. While we have made several assumptions in Eq. (B1), it should be straightforward to translate this limit to other more specific scenarios.

[1] G. Bertone, D. Hooper, and J. Silk, Particle dark matter: Evidence, candidates and constraints, Phys. Rep. **405**, 279 (2005).
[2] L. E. Strigari, Galactic searches for dark matter, Phys. Rep. **531**, 1 (2013).
[3] M. R. Buckley and A. H. G. Peter, Gravitational probes of dark matter physics, Phys. Rep. **761**, 1 (2018).
[4] A. Kusenko, Sterile neutrinos: The dark side of the light fermions, Phys. Rep. **481**, 1 (2009).
[5] R. Adhikari *et al.*, A white paper on keV sterile neutrino dark matter, J. Cosmol. Astropart. Phys. 01 (2017) 025.
[6] K. N. Abazajian, Sterile neutrinos in cosmology, Phys. Rep. **711-712**, 1 (2017).
[7] A. Boyarsky, M. Drewes, T. Lasserre, S. Mertens, and O. Ruchayskiy, Sterile neutrino dark matter, Prog. Part. Nucl. Phys. **104**, 1 (2019).
[8] R. Shrock, Decay l0 —¿ nu(lepton) gamma in gauge theories of weak and electromagnetic interactions, Phys. Rev. D **9**, 743 (1974).
[9] P. B. Pal and L. Wolfenstein, Radiative decays of massive neutrinos, Phys. Rev. D **25**, 766 (1982).
[10] A. D. Dolgov and S. H. Hansen, Massive sterile neutrinos as warm dark matter, Astropart. Phys. **16**, 339 (2002).
[11] K. Abazajian, G. M. Fuller, and W. H. Tucker, Direct detection of warm dark matter in the x-ray, Astrophys. J. **562**, 593 (2001).
[12] S. Dodelson and L. M. Widrow, Sterile-Neutrinos as Dark Matter, Phys. Rev. Lett. **72**, 17 (1994).
[13] X.-D. Shi and G. M. Fuller, A New Dark Matter Candidate: Nonthermal Sterile Neutrinos, Phys. Rev. Lett. **82**, 2832 (1999).
[14] M. Shaposhnikov and I. Tkachev, The nuMSM, inflation, and dark matter, Phys. Lett. B **639**, 414 (2006).
[15] A. Kusenko, Sterile Neutrinos, Dark Matter, and the Pulsar Velocities in Models with a Higgs Singlet, Phys. Rev. Lett. **97**, 241301 (2006).
[16] K. Petraki and A. Kusenko, Dark-matter sterile neutrinos in models with a gauge singlet in the Higgs sector, Phys. Rev. D **77**, 065014 (2008).
[17] A. Merle, V. Niro, and D. Schmidt, New production mechanism for keV sterile neutrino dark matter by decays of frozen-in scalars, J. Cosmol. Astropart. Phys. 03 (2014) 028.
[18] M. Frigerio and C. E. Yaguna, Sterile neutrino dark matter and low scale leptogenesis from a charged scalar, Eur. Phys. J. C **75**, 31 (2015).
[19] L. Lello and D. Boyanovsky, Cosmological implications of light sterile neutrinos produced after the QCD phase transition, Phys. Rev. D **91**, 063502 (2015).
[20] A. Merle and M. Totzauer, keV sterile neutrino dark matter from singlet scalar decays: Basic concepts and subtle features, J. Cosmol. Astropart. Phys. 06 (2015) 011.
[21] A. V. Patwardhan, G. M. Fuller, C. T. Kishimoto, and A. Kusenko, Diluted equilibrium sterile neutrino dark matter, Phys. Rev. D **92**, 103509 (2015).
[22] M. Fukugita and T. Yanagida, Baryogenesis without grand unification, Phys. Lett. B **174**, 45 (1986).
[23] T. Asaka, S. Blanchet, and M. Shaposhnikov, The nuMSM, dark matter and neutrino masses, Phys. Lett. B **631**, 151 (2005).
[24] T. Asaka, M. Laine, and M. Shaposhnikov, Lightest sterile neutrino abundance within the nuMSM, J. High Energy Phys. 01 (2007) 091; Erratum, J. High Energy Phys. 02 (2015) 28.
[25] L. Canetti, M. Drewes, and M. Shaposhnikov, Sterile Neutrinos as the Origin of Dark and Baryonic Matter, Phys. Rev. Lett. **110**, 061801 (2013).
[26] L. Canetti, M. Drewes, T. Frossard, and M. Shaposhnikov, Dark matter, baryogenesis and neutrino oscillations from right handed neutrinos, Phys. Rev. D **87**, 093006 (2013).
[27] C. R. Watson, J. F. Beacom, H. Yuksel, and T. P. Walker, Direct x-ray constraints on sterile neutrino warm dark matter, Phys. Rev. D **74**, 033009 (2006).

[28] M. Loewenstein, A. Kusenko, and P. L. Biermann, New limits on sterile neutrinos from Suzaku observations of the Ursa Minor Dwarf spheroidal galaxy, Astrophys. J. **700**, 426 (2009).
[29] H. Yuksel, J. F. Beacom, and C. R. Watson, Strong Upper Limits on Sterile Neutrino Warm Dark Matter, Phys. Rev. Lett. **101**, 121301 (2008).
[30] A. Boyarsky, D. Malyshev, A. Neronov, and O. Ruchayskiy, Constraining DM properties with SPI, Mon. Not. R. Astron. Soc. **387**, 1345 (2008).
[31] A. Boyarsky, D. Iakubovskyi, O. Ruchayskiy, and V. Savchenko, Constraints on decaying dark matter from XMM-Newton observations of M31, Mon. Not. R. Astron. Soc. **387**, 1361 (2008).
[32] S. Riemer-Sørensen and S. H. Hansen, Decaying dark matter in Draco, Astron. Astrophys. **500**, L37 (2009).
[33] S. Horiuchi, P. J. Humphrey, J. Onorbe, K. N. Abazajian, M. Kaplinghat, and S. Garrison-Kimmel, Sterile neutrino dark matter bounds from galaxies of the local group, Phys. Rev. D **89**, 025017 (2014).
[34] E. Bulbul, M. Markevitch, A. Foster, R. K. Smith, M. Loewenstein, and S. W. Randall, Detection of an unidentified emission line in the stacked x-ray spectrum of galaxy clusters, Astrophys. J. **789**, 13 (2014).
[35] A. Boyarsky, O. Ruchayskiy, D. Iakubovskyi, and J. Franse, Unidentified Line in X-Ray Spectra of the Andromeda Galaxy and Perseus Galaxy Cluster, Phys. Rev. Lett. **113**, 251301 (2014).
[36] S. Riemer-Sørensen, Constraints on the presence of a 3.5 keV dark matter emission line from Chandra observations of the Galactic Centre, Astron. Astrophys. **590**, A71 (2016).
[37] T. E. Jeltema and S. Profumo, Discovery of a 3.5 keV line in the Galactic Centre and a critical look at the origin of the line across astronomical targets, Mon. Not. R. Astron. Soc. **450**, 2143 (2015).
[38] A. Boyarsky, J. Franse, D. Iakubovskyi, and O. Ruchayskiy, Checking the Dark Matter Origin of a 3.53 keV Line with the Milky Way Center, Phys. Rev. Lett. **115**, 161301 (2015).
[39] D. Malyshev, A. Neronov, and D. Eckert, Constraints on 3.55 keV line emission from stacked observations of dwarf spheroidal galaxies, Phys. Rev. D **90**, 103506 (2014).
[40] M. E. Anderson, E. Churazov, and J. N. Bregman, Non-detection of x-ray emission from sterile neutrinos in stacked Galaxy spectra, Mon. Not. R. Astron. Soc. **452**, 3905 (2015).
[41] O. Urban, N. Werner, S. W. Allen, A. Simionescu, J. S. Kaastra, and L. E. Strigari, A Suzaku search for dark matter emission lines in the x-ray brightest galaxy clusters, Mon. Not. R. Astron. Soc. **451**, 2447 (2015).
[42] T. Tamura, R. Iizuka, Y. Maeda, K. Mitsuda, and N. Y. Yamasaki, An x-ray spectroscopic search for dark matter in the Perseus cluster with Suzaku, Publ. Astron. Soc. Jpn. **67**, 23 (2015).
[43] N. Sekiya, N. Y. Yamasaki, and K. Mitsuda, A search for a keV signature of radiatively decaying dark matter with Suzaku XIS observations of the x-ray diffuse background, Publ. Astron. Soc. Jpn. **68**, S31 (2016).
[44] E. Figueroa-Feliciano *et al.* (XQC Collaboration), Searching for keV sterile neutrino dark matter with x-ray microcalorimeter sounding rockets, Astrophys. J. **814**, 82 (2015).
[45] S. Riemer-Sørensen *et al.*, Dark matter line emission constraints from NuSTAR observations of the bullet cluster, Astrophys. J. **810**, 48 (2015).
[46] D. Iakubovskyi, E. Bulbul, A. R. Foster, D. Savchenko, and V. Sadova, Testing the origin of 3.55 keV line in individual galaxy clusters observed with XMM-Newton, arXiv:1508.05186.
[47] T. E. Jeltema and S. Profumo, Deep XMM Observations of Draco rule out at the 99% confidence level a dark matter decay origin for the 3.5 keV line, Mon. Not. R. Astron. Soc. **458**, 3592 (2016).
[48] O. Ruchayskiy, A. Boyarsky, D. Iakubovskyi, E. Bulbul, D. Eckert, J. Franse, D. Malyshev, M. Markevitch, and A. Neronov, Searching for decaying dark matter in deep XMMNewton observation of the Draco Dwarf spheroidal, Mon. Not. R. Astron. Soc. **460**, 1390 (2016).
[49] J. Franse *et al.*, Radial profile of the 3.55 keV line out to R_{200} in the Perseus cluster, Astrophys. J. **829**, 124 (2016).
[50] E. Bulbul, M. Markevitch, A. Foster, E. Miller, M. Bautz, M. Loewenstein, S. W. Randall, and R. K. Smith, Searching for the 3.5 keV line in the stacked Suzaku observations of Galaxy clusters, Astrophys. J. **831**, 55 (2016).
[51] F. Hofmann, J. S. Sanders, K. Nandra, N. Clerc, and M. Gaspari, 7.1 keV sterile neutrino constraints from x-ray observations of 33 clusters of galaxies with Chandra ACIS, Astron. Astrophys. **592**, A112 (2016).
[52] A. Neronov, D. Malyshev, and D. Eckert, Decaying dark matter search with NuSTAR deep sky observations, Phys. Rev. D **94**, 123504 (2016).
[53] F. A. Aharonian *et al.* (Hitomi Collaboration), Hitomi constraints on the 3.5 keV line in the Perseus galaxy cluster, Astrophys. J. **837**, L15 (2017).
[54] K. Perez, K. C. Y. Ng, J. F. Beacom, C. Hersh, S. Horiuchi, and R. Krivonos, Almost closing the MSM sterile neutrino dark matter window with NuSTAR, Phys. Rev. D **95**, 123002 (2017).
[55] N. Cappelluti, E. Bulbul, A. Foster, P. Natarajan, M. C. Urry, M. W. Bautz, F. Civano, E. Miller, and R. K. Smith, Searching for the 3.5 keV line in the deep fields with Chandra: The 10 Ms observations, Astrophys. J. **854**, 179 (2018).
[56] T. Tamura *et al.*, An x-ray spectroscopic search for dark matter and unidentified line signatures in the Perseus cluster with Hitomi, arXiv:1811.05767.
[57] K. N. Abazajian, Resonantly Produced 7 keV Sterile Neutrino Dark Matter Models and the Properties of Milky Way Satellites, Phys. Rev. Lett. **112**, 161303 (2014).
[58] D. P. Finkbeiner and N. Weiner, X-ray line from exciting dark matter, Phys. Rev. D **94**, 083002 (2016).
[59] T. Higaki, K. S. Jeong, and F. Takahashi, The 7 keV axion dark matter and the x-ray line signal, Phys. Lett. B **733**, 25 (2014).
[60] V. Brdar, J. Kopp, J. Liu, and X.-P. Wang, X-Ray Lines from Dark Matter Annihilation at the keV Scale, Phys. Rev. Lett. **120**, 061301 (2018).

[61] M. H. Namjoo, T. R. Slatyer, and C.-L. Wu, Enhanced n-body annihilation of dark matter and its indirect signatures, arXiv:1810.09455.

[62] K. Nakayama, F. Takahashi, and T. T. Yanagida, Revisiting the number-theory dark matter scenario and the weak gravity conjecture, Phys. Lett. B **790**, 218 (2019).

[63] L. Gu, J. Kaastra, A. J. J. Raassen, P. D. Mullen, R. S. Cumbee, D. Lyons, and P. C. Stancil, A novel scenario for the possible x-ray line feature at 3.5 keV: Charge exchange with bare sulfur ions, Astron. Astrophys. **584**, L11 (2015).

[64] L. Gu, J. Mao, J. de Plaa, A. J. J. Raassen, C. Shah, and J. S. Kaastra, Charge exchange in galaxy clusters, Astron. Astrophys. **611**, A26 (2018).

[65] K. Nandra *et al.*, The hot and energetic Universe: A white paper presenting the science theme motivating the Athena+ mission, arXiv:1306.2307.

[66] T. Kitayama *et al.*, ASTRO-H white paper–Clusters of galaxies and related science, arXiv:1412.1176.

[67] E. G. Speckhard, K. C. Y. Ng, J. F. Beacom, and R. Laha, Dark Matter Velocity Spectroscopy, Phys. Rev. Lett. **116**, 031301 (2016).

[68] D. Powell, R. Laha, K. C. Y. Ng, and T. Abel, Doppler effect on indirect detection of dark matter using dark matter only simulations, Phys. Rev. D **95**, 063012 (2017).

[69] C. Dessert, N. L. Rodd, and B. R. Safdi, Evidence against the decaying dark matter interpretation of the 3.5 keV line from blank sky observations, arXiv:1812.06976.

[70] A. Boyarsky, D. Iakubovskyi, O. Ruchayskiy, and D. Savchenko, Surface brightness profile of the 3.5 keV line in the Milky Way halo, arXiv:1812.10488.

[71] A. Boyarsky, A. Neronov, O. Ruchayskiy, M. Shaposhnikov, and I. Tkachev, Where to Find a Dark Matter Sterile Neutrino?, Phys. Rev. Lett. **97**, 261302 (2006).

[72] K. C. Y. Ng, S. Horiuchi, J. M. Gaskins, M. Smith, and R. Preece, Improved limits on sterile neutrino dark matter using full-sky Fermi gamma-ray burst monitor data, Phys. Rev. D **92**, 043503 (2015).

[73] D. R. Wik *et al.*, NuSTAR observations of the bullet cluster: Constraints on inverse Compton emission, Astrophys. J. **792**, 48 (2014).

[74] F. A. Harrison *et al.*, The nuclear spectroscopic telescope array (NuSTAR) high-energy x-ray mission, Astrophys. J. **770**, 103 (2013).

[75] K. K. Madsen *et al.*, Calibration of the NuSTAR high energy focusing x-ray telescope, Astrophys. J. Suppl. Ser. **220**, 8 (2015).

[76] K. Z. Stanek and P. M. Garnavich, Distance to M31 with the HST and HIPPARCOS red clump stars, Astrophys. J. **503**, L131 (1998).

[77] S. Holland, The distance to the M31 globular cluster system, Astron. J. **115**, 1916 (1998).

[78] M. Lazzarini *et al.*, Young accreting compact objects in M31: The combined power of NuSTAR, Chandra, and Hubble, Astrophys. J. **862**, 28 (2018).

[79] H. Stiele and A. K. H. Kong, NuSTAR view of the central region of M31, Mon. Not. R. Astron. Soc. **475**, 4911 (2018).

[80] A. Tamm, E. Tempel, P. Tenjes, O. Tihhonova, and T. Tuvikene, Stellar mass map and dark matter distribution in M31, Astron. Astrophys. **546**, A4 (2012).

[81] H. Stiele, W. Pietsch, F. Haberl, D. Hatzidimitriou, R. Barnard, B. F. Williams, A. K. H. Kong, and U. Kolb, The deep XMM-Newton survey of M31, Astron. Astrophys. **534**, A55 (2011).

[82] XMM-Newton Science Data Images–M31 Galaxy, https://heasarc.gsfc.nasa.gov/docs/xmm/gallery/esas-gallery/xmm_gal_science_m31.html.

[83] D. E. Gruber, J. L. Matteson, L. E. Peterson, and G. V. Jung, The spectrum of diffuse cosmic hard x-rays measured with HEAO-1, Astrophys. J. **520**, 124 (1999).

[84] E. Churazov *et al.*, INTEGRAL observations of the cosmic x-ray background in the 5–100 keV range via occultation by the Earth, Astron. Astrophys. **467**, 529 (2006).

[85] R. G. West, C. R. Barber, and E. L. Folgheraiter, Diffuse soft x-ray emission in ROSAT observations of M31, Mon. Not. R. Astron. Soc. **287**, 10 (1997).

[86] Á. Bogdán and M. Gilfanov, Unresolved x-ray emission in M31 and constraints on progenitors of classical novae, Mon. Not. R. Astron. Soc. **405**, 209 (2010).

[87] S. Trudolyubov, O. Kotov, W. Priedhorsky, F. Cordova, and K. Mason, XMM-Newton observations of the M31 northern disk: Properties of selected x-ray sources and diffuse emission, Astrophys. J. **634**, 314 (2005).

[88] E. Anders and N. Grevesse, Abundances of the elements: Meteoritic and solar, Geochim. Cosmochim. Acta **53**, 197 (1989).

[89] M. Bałucińska-Church and D. McCammon, Photoelectric absorption cross sections with variable abundances, Astrophys. J. **400**, 699 (1992).

[90] M. Yan, H. R. Sadeghpour, and A. Dalgarno, Photoionization cross sections of He and H_2, Astrophys. J. **496**, 1044 (1998).

[91] R. Braun, D. A. Thilker, R. A. M. Walterbos, and E. Corbelli, A wide-field high-resolution H I mosaic of Messier 31. I. opaque atomic gas and star formation rate density, Astrophys. J. **695**, 937 (2009).

[92] P. Predehl and J. H. M. M. Schmitt, X-raying the interstellar medium: ROSAT observations of dust scattering halos, Astron. Astrophys. **293**, 889 (1995).

[93] J. M. Dickey and F. J. Lockman, HI in the galaxy, Annu. Rev. Astron. Astrophys. **28**, 215 (1990).

[94] P. M. W. Kalberla, W. B. Burton, D. Hartmann, E. M. Arnal, E. Bajaja, R. Morras, and W. G. L. Poppel, The Leiden/Argentine/Bonn (LAB) survey of Galactic HI: Final data release of the combined LDS and IAR surveys with improved stray-radiation corrections, Astron. Astrophys. **440**, 775 (2005).

[95] F. Calore, N. Bozorgnia, M. Lovell, G. Bertone, M. Schaller, C. S. Frenk, R. A. Crain, J. Schaye, T. Theuns, and J. W. Trayford, Simulated Milky Way analogues: Implications for dark matter indirect searches, J. Cosmol. Astropart. Phys. 12 (2015) 053.

[96] R. Yunis, C. R. Argelles, Nick E. Mavromatos, A. Molin, A. Krut, J. A. Rueda, and R. Ruffini, New constraints on sterile neutrino dark matter from the Galactic Center, arXiv:1810.05756.

[97] J. F. Cherry and S. Horiuchi, Closing in on resonantly produced sterile neutrino dark matter, Phys. Rev. D **95**, 083015 (2017).

[98] A. D. Dolgov, S. H. Hansen, S. Pastor, S. T. Petcov, G. G. Raffelt, and D. V. Semikoz, Cosmological bounds on neutrino degeneracy improved by flavor oscillations, Nucl. Phys. **B632**, 363 (2002).

[99] P. D. Serpico and G. G. Raffelt, Lepton asymmetry and primordial nucleosynthesis in the era of precision cosmology, Phys. Rev. D **71**, 127301 (2005).

[100] A. Boyarsky, O. Ruchayskiy, and M. Shaposhnikov, The role of sterile neutrinos in cosmology and astrophysics, Annu. Rev. Nucl. Part. Sci. **59**, 191 (2009).

[101] T. Venumadhav, F.-Y. Cyr-Racine, K. N. Abazajian, and C. M. Hirata, Sterile neutrino dark matter: Weak interactions in the strong coupling epoch, Phys. Rev. D **94**, 043515 (2016).

[102] S. Horiuchi, B. Bozek, K. N. Abazajian, M. Boylan-Kolchin, J. S. Bullock, S. Garrison-Kimmel, and J. Onorbe, Properties of resonantly produced sterile neutrino dark matter subhaloes, Mon. Not. R. Astron. Soc. **456**, 4346 (2016).

[103] B. Bozek, M. Boylan-Kolchin, S. Horiuchi, S. Garrison-Kimmel, K. Abazajian, and J. S. Bullock, Resonant sterile neutrino dark matter in the local and high-z universe, Mon. Not. R. Astron. Soc. **459**, 1489 (2016).

[104] M. R. Lovell, V. Gonzalez-Perez, S. Bose, A. Boyarsky, S. Cole, C. S. Frenk, and O. Ruchayskiy, Addressing the too big to fail problem with baryon physics and sterile neutrino dark matter, Mon. Not. R. Astron. Soc. **468**, 2836 (2017).

[105] A. Schneider, Astrophysical constraints on resonantly produced sterile neutrino dark matter, J. Cosmol. Astropart. Phys. 04 (2016) 059.

[106] J. Baur, N. Palanque-Delabrouille, C. Yeche, A. Boyarsky, O. Ruchayskiy, r. Armengaud, and J. Lesgourgues, Constraints from Ly-α forests on non-thermal dark matter including resonantly-produced sterile neutrinos, J. Cosmol. Astropart. Phys. 12 (2017) 013.

[107] S. Tremaine and J. E. Gunn, Dynamical Role of Light Neutral Leptons in Cosmology, Phys. Rev. Lett. **42**, 407 (1979).

[108] E. Jones, T. Oliphant, P. Peterson *et al.*, SciPy: Open source scientific tools for Python, http://www.scipy.org/.

[109] T. P. Robitaille *et al.* (Astropy Collaboration), Astropy: A community Python package for astronomy, Astron. Astrophys. **558**, A33 (2013).

[110] A. M. Price-Whelan *et al.* (Astropy Collaboration), The Astropy project: Building an open-science project and status of the v2.0 core package, Astron. J. **156**, 123 (2018).

[111] R. K. Leane, T. R. Slatyer, J. F. Beacom, and K. C. Y. Ng, GeV-scale thermal WIMPs: Not even slightly ruled out, Phys. Rev. D **98**, 023016 (2018).

[112] K. C. Y. Ng, R. Laha, S. Campbell, S. Horiuchi, B. Dasgupta, K. Murase, and J. F. Beacom, Resolving small-scale dark matter structures using multisource indirect detection, Phys. Rev. D **89**, 083001 (2014).

[113] N. Hiroshima, S. Ando, and T. Ishiyama, Modeling evolution of dark matter substructure and annihilation boost, Phys. Rev. D **97**, 123002 (2018).